COMMUNICATION

Semiconducting Carbon Nanotubes as Crystal Growth Templates and Grain Bridges in Perovskite Solar Cells

Received 00th January 20xx,
Accepted 00th January 20xx

DOI: 10.1039/x0xx00000x

Seungju Seo,‡[a] Il Jeon,‡*[a] Rong Xiang,[a] Changsoo Lee,[b] Hao Zhang,[a] Takeshi Tanaka,[c] Jin-Wook Lee,[d] Donguk Suh,[a] Tatsuro Ogamoto,[a] Ryosuke Nishikubo,[e] Akinori Saeki,[e] Shohei Chiashi,[a] Junichiro Shiomi,[a] Hiromichi Kataura,[c] Hyuck Mo Lee,[b] Yang Yang,[d] Yutaka Matsuo*[a,f] and Shigeo Maruyama*[a,g]

Grain size control and boundary passivation of perovskite films are the key to obtaining highly efficient perovskite solar cells. In order to accomplish both goals, semiconducting single-walled carbon nanotubes are added to perovskite films as additives, functioning both the crystal growth templates and charge bridges between the perovskite grains. The resulting perovskite films display more uniform and larger crystal grains compared with conventional films owing to long and flexible single-walled carbon nanotubes, retarding the crystal growth and functioning as the cross-linker between perovskite grains. In addition, sodium deoxycholates attached on the carbon nanotubes passivated the grain boundaries by forming Lewis adducts. Thanks to the improved quality of the photoactive layers by using semiconducting carbon nanotubes, a power conversion efficiency of 19.5% was obtained which is higher than 18.1% of reference devices with no additives.

Perovskite solar cells (PSCs)[1–4] have drawn much attention as an alternative energy source owing to the high absorption coefficient,[5] long-range diffusion length,[6] and high defect tolerance[7] of the lead-halide perovskite photoactive layer. Although PSCs are considered to be promising next-generation solar devices, further breakthroughs in terms of power conversion efficiency (PCE) are necessary to supersede conventional silicon solar cells. In this regard, control of grain size and passivation of its defective boundaries are the key to obtaining high PCE.[8–10] To increase the grain size, inducing homogeneous nucleation and retarding perovskite crystal growth are important.[11–13] Accordingly, polymer templates[14,15] and various anti-solvents[16] have been developed to achieve these. For the passivation of grain boundaries, Lewis adduction formation at the grain surface has a favourable effect as structural disorders in the interface of the grains induce shallow trap states, which lead to non-radiative recombination of localized charge carriers.[17–20] Ideally, technologies aiming at controlling the grain size and passivating the grain interfaces at the same time are desired.[21–23]

Over the last two decades, carbon nanotubes have generated a lot of excitement among researchers for their device applicability on account of their exceptional charge carrier transporting property, and outstanding chemical and mechanical stability. In particular, semiconducting single-walled carbon nanotubes (s-SWNTs) with a direct bandgap of up to 2 eV show high conductivity along the tube axis, qualifying for charge-transporting media in PSCs.[24–26] Recently, fullerene has been reported to function as charge-transporters in PSCs.[27,28] However, fullerenes have lower carrier mobility and stability than SWNTs that they cannot be considered an ideal choice of materials.[29] To date, there has been one report on the application of pure s-SWNTs in PSCs, where s-SWNTs were used as a charge extractor next to a perovskite active layer.[30] Another close application is sulfonated multi-walled carbon nanotubes as crystal growth templates inside a perovskite film, but the carbon nanotubes were not semiconducting as they were multi-walled.[31]

Herein, we demonstrate purified s-SWNTs dispersed in water functioning as both the perovskite crystal growth templates and charge transporters inside a perovskite layer, increasing the PCE of PSCs from 18.1% to 19.5%. Sodium deoxycholate (DOC) surfactants were used to collect s-SWNTs bound to agarose gel in the process of separation. The carbonyl groups in DOC formed Lewis adducts with perovskite precursors to function as growth templates and passivators, inducing large crystal size and reducing trap sites, respectively. Since s-SWNTs had to be dispersed in water for a purification step, a small amount of water was added into a $CH_3NH_3PbI_3$ ($MAPbI_3$) solution. To identify the role of added water, we fabricated water-added

[a] *Department of Mechanical Engineering, The University of Tokyo, 7-3-1 Hongo, Bunkyo-ku, Tokyo 113-8656, Japan.*
[b] *Department of Materials Science and Engineering, KAIST, 291 Daehak-ro, Yuseong-gu, Daejeon, 34141, Republic of Korea*
[c] *Nanomaterials Research Institute, National Institute of Advanced Industrial Science and Technology (AIST), Tsukuba, Ibaraki 305-8565, Japan.*
[d] *Department of Materials Science and Engineering, University of California, Los Angeles, Los Angeles, CA 90095, USA.*
[e] *Department of Applied Chemistry, Osaka University, Osaka, 565-0871 Japan.*
[f] *Hefei National Laboratory for Physical Sciences at the Microscale, University of Science and Technology of China, Hefei, Anhui 230026, China.*
[g] *Energy NanoEngineering Lab., National Institute of Advanced Industrial Science and Technology (AIST), Tsukuba, Ibaraki 305-8564, Japan.*

† Electronic Supplementary Information (ESI) available: Experimental section, Pictures of s-SWNT dispersion in water, Chiral mappings, AFM images of s-SWNTs, Cross-sectional SEM images of PSCs, J–V data, Photovoltaic parameter statistical analysis, IPCE data, MPPT data, Supporting PSC device data, ESEM images of perovskite film growth, XRD, PL, and c-AFM images of perovskite films. See DOI: 10.1039/x0xx00000x

‡ These authors contributed equally.

PSCs for a comparison. The added water enhanced the quality of the perovskite crystal grains in terms of homogeneity. With the presence of s-SWNTs, the size of crystal grains and mobility of the perovskite film increased. This was verified by microscopic techniques, such as scanning electron microscopy (SEM) and in-situ transmission electron microscope (TEM), and various charge kinetics measurements. Nevertheless, there was a limitation in the use of s-SWNT$_{(aq)}$; it was found that 2wt% of s-SWNT$_{(aq)}$ was the optimal amount and higher concentration resulted in the decrease in device performance. We ascribed this to the limited purity s-SWNTs and low mobility of DOC surfactants. Subsequently, this leaves us with the room for further improvement by the purity of s-SWNTs and the mobility of surfactants, which are future work to follow.

RESULTS AND DISCUSSION

Metallic carbon nanotubes functions as recombination sites in perovskite film and forms Schottky junctions with neighbouring semiconducting carbon nanotubes. Therefore, it is important that we use highly pure s-SWNTs if we are to use them inside the perovskite film.[28,32,33] We obtained highly pure s-SWNTs by agarose gel chromatography, where the s-SWNTs were selectively adsorbed to the gel in 1% SDS and were eluted by 1% DOC (Fig. S1). Details can be checked in ESI. The photoluminescence (PL) mapping (Fig. 1a, Fig S2) and the corresponding chirality mapping (Fig. 1b, Table S1) show that there are s-SWNTs in the attained solution with the major chirality being (9,4). The UV-Vis-NIR spectrum with strong S11 and S22 transition peaks corroborate the high purity of s-SWNTs (Fig. 1c). Moreover, the Raman spectra obtained from 785 nm and 633 nm laser lines substantiate the s-SWNT purity (Fig. 1d). Atomic force microscopy (AFM) images of the s-SWNTs drop-casted on glass substrates show that the SWNTs are longer than 1 µm and possess an entangled geometry. This means that the tubes are long and flexible enough to encompass the perovskite crystal grains (Fig. S3). The fact that the SWNT strings appear thicker than the measured diameters indicates that many tubes exist in bundles.

$MAPbI_3$ solutions containing different concentrations of the s-SWNT$_{(aq)}$ were used for PSC fabrication (Fig. 1e, Fig. S4). The performance of s-SWNT-added PSCs were compared with that of conventional PSCs and water-added PSCs to differentiate the effect of s-SWNTs from water. The conventional PSCs exhibited a PCE of 18.1% with the short-circuit current (J_{SC}) of 23.1 mA cm^{-2}, the open-circuit voltage (V_{OC}) of 1.06 V, and the fill factor (FF) of 0.74 (Table 1, Fig. 1f, Fig. S5, S6, S7, and S8). The water-added PSCs showed a higher PCE of 18.7% with the J_{SC} of 22.9 mA cm^{-2}, V_{OC} of 1.08 V, and FF of 0.76. The s-SWNT$_{(aq)}$-added PSCs showed an even higher PCE of 19.5% with the J_{SC} of 23.7 mA cm^{-2}, V_{OC} of 1.14 V, and FF of 0.72. Water-added PSCs have

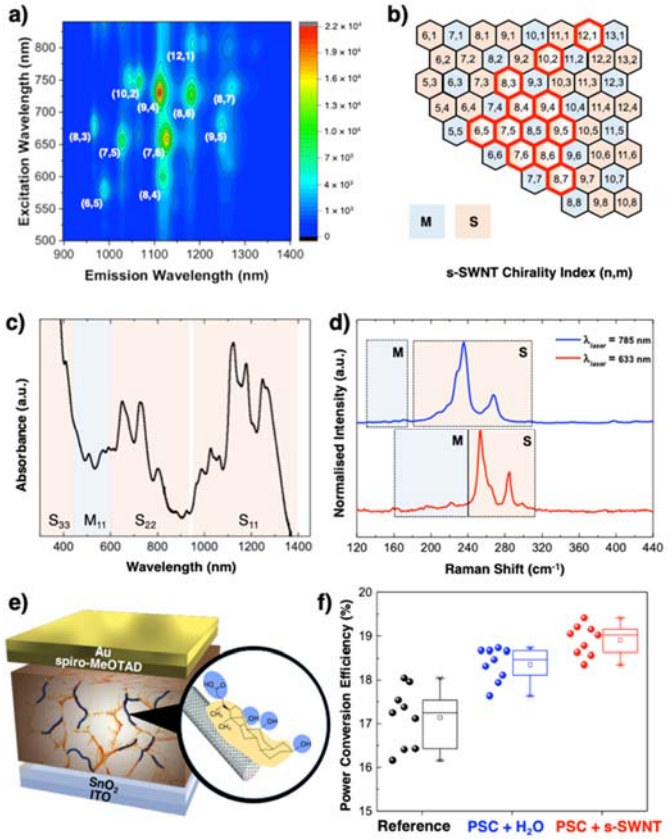

Fig .1 (a) PL mapping of the purified s-SWNTs. (b) Chirality index mapping of the s-SWNT solution with the corresponding chirality marked with red colour. (c) UV-Vis-NIR Absorption spectroscopy of the s-SWNTs. (d) Raman spectroscopy of the s-SWNTs under the 785 nm laser line (blue) and 633 nm laser line (red). (e) Structure of the PSC fabricated in this work with an illustration of s-SWNT with an attached DOC surfactant. (f) Statistical analysis data of obtained PCEs from the reference devices (black), the water-added devices (blue), and the s-SWNT-added devices (red).

previously been reported to exhibit higher PCEs than reference devices in both inverted-type[34–37] and normal-type[38,39] PSCs owing to improved perovskite film morphology and coverage. While the reported optimal concentration of the water additive differs among the literatures, 2 wt% was the optimal concentration in our case (Table S2). The same was true for the s-SWNT$_{(aq)}$-added PSCs. A concentration of 2 wt% gave the highest device performance (Table 2). A notable difference in the photovoltaic parameters between the s-SWNT-added PSCs and the water-added PSCs was that the s-SWNT-added PSCs exhibited higher J_{SC} and V_{OC}, but lower FF. Consequently, we conjectured that the s-SWNTs possibly functioned as an effective additive improving the crystal quality and charge carrier dynamics in the device. The decrease in FF was cause by the increase in R_S, indicating possible hinderance in charge flow upon the addition of s-SWNT.

From the AFM images and their roughness average (R_a) values, we can observe that the conventional perovskite films display rough and inhomogeneous grain sizes (Fig. 2a - c). The water-added perovskite films show more uniform crystal grains, which are in agreement with the previous reports (Fig. 2b).[34–37] The s-SWNT-added perovskite films show a much larger grain size with decreased grain boundaries (Fig. 2c), implying influence of s-SWNTs on the crystal growth of the film. This explains the high J_{SC} values of the s-SWNT-added PSCs compared with the water-added PSCs and the reference devices, because large perovskite grains have known to render high J_{SC} values. Furthermore, our incident photon to current efficiency (IPCE) data show that there is higher IPCE values in the lower wavelength region between 350 nm to 450 nm (Fig. S7). We surmise this to be from the excitation in s-SWNTs as they correspond with the band gaps of the chiralities found in Figure 1 a and 1b. Thus, the s-SWNTs may have also contributed to the high J_{SC}. SEM and TEM were conducted on the s-SWNT-added perovskite films to analyse the s-SWNTs in the perovskite grain boundaries. TEM image of the perovskite grain boundary (Zone 1) in Figure 2d shows that there are non-crystalline substances found at the surface of perovskite grains (Fig. 2e). These are suspected to be s-SWNTs and DOCs. There seems to be DOC aggregations (Zone 2), and sometimes a large aggregation which probably contains both DOCs and s-SWNTs as a bundle (Zone 3). Some images show a long trail of s-SWNT along the perovskite grain, which are likely to be single strings of s-SWNTs passivating the grain boundary (Fig. 2f and S9b, d). The fast Fourier transform (FFT) analysis supports our point as the perovskite grain area has a cubic phase crystal with a spacing of approximately 3 Å, whereas the s-SWNT and DOC areas are totally amorphous. Such amorphous aggregations were not observed in reference perovskite (Fig. S9a, c). To understand the influence of the added water and s-SWNT on the perovskite crystal growth, environmental SEM (ESEM) was used to observe the perovskite crystal growth in-situ. It is worth noting that due to the vacuum environment of the ESEM set up, actual crystal nucleation and growth condition in ambience will be different. Therefore, the data is valid only for the comparison between the different experimental splits. Figure S10 shows that the water-added perovskite films demonstrate much more uniform and circular perovskite seeds with slower growth rate than the reference films. This implies that the water additive influences from the seed formation to the growth rate, which lead to a better morphology of the perovskite films. The s-SWNT-added perovskite films also display uniform and circular seeds owing to the added water, but the crystals are much larger and the crystal growth is slower compared with that of the water-added perovskite film.[14,40] This proves that the added s-SWNTs function as crystal growth templates. Illustration in Figure 2g depicts how the added water and s-SWNTs interact during the perovskite film formation. This is deduced from our density functional theory (DFT) calculation of interactions of Lewis

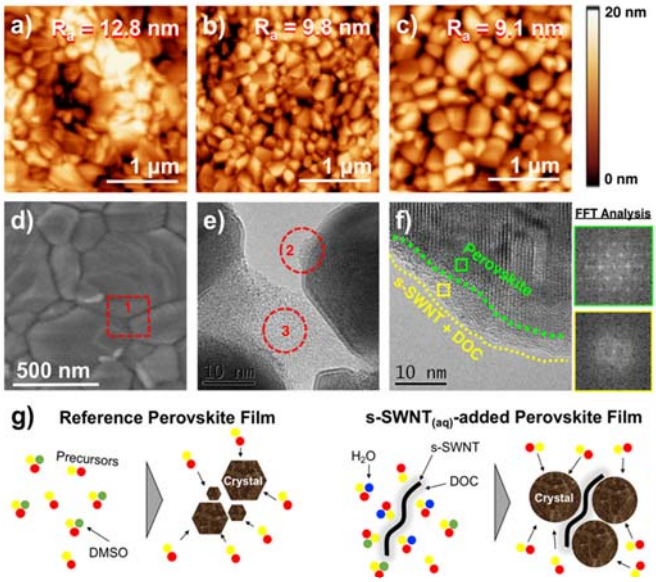

Fig .2 AFM images of (a) the reference MAPbI3 film, (b) the water-added MAPbI3 film, and (c) the s-SWNT-added MAPbI3 film. (d) SEM image and (e)(f) TEM images of the s-SWNT-added MAPbI3 film with the FFT analysis as insets. (g) Illustration depicting the role of water and s-SWNT additives during the perovskite growth of the s-SWNT-added MAPbI3 film compared with the reference.

bases, namely, dimethyl sulfoxide (DMSO), water, methylammonium ion (MA), and DOC on Pb^{2+} (Fig. S11). The calculation results show that the interaction between DOC and Pb^{2+} is stronger compared to DMSO and water (Table S3). This means that DOC can effectively raise the nucleation energy, ΔG to slow down the crystal growth better than either DMSO or water. The ability for s-SWNTs to function as the crystal growth template comes from the Lewis base carbonyl groups with lone pair electrons on DOC, interacting with the nucleation sites of the Lewis acid perovskite precursors perovskite precursors.[19,41] This is an interesting concept as none of the reported s-SWNT applications to perovskite material does not involve surfactants, to the best of our knowledge.[42,43] Fourier-transform infrared (FTIR) spectroscopy data reveals that the C=O bond absorption peak of DOC powder at 1,560 cm^{-1} shifted to a lower vibration upon addition of PbI_2 (Fig. 3a).[44] The weakened C=O bond strength of DOCs indicates the formation of SWNT–DOC–PbI_2 adducts by formation of a dative bond mediated from the lone pair electrons on C=O. The formation of such adducts retards the crystal growth by elevating nucleation barrier of perovskite nuclei, thereby increasing the size of perovskite crystal grains.[45] Unlike dimethyl sulfoxide (DMSO), DOCs on SWNTs do not evaporate during the annealing step of the perovskite films, which implies that SWNT-DOCs remain in the films after completion of the crystal growth. As illustrated in Fig. 2g, the SWNT-DOCs and their adducts are probably repelled to the grain boundaries as the grain gets larger, subsequently sitting at the grain boundaries. X-ray diffraction spectroscopy (XRD) confirms the increase in the grain size and the passivation of the grain boundaries (Fig. S12 and S14, Table S4 and S5). The XRD spectra of the perovskite films indicate a tetragonal phase with a dominant (110) peak at

14.1°. The crystal grain size can be estimated from full-width at half-maximum (FWHM) of the (110) peaks using the Debye – Scherrer equation.[46] The reference film, the water-added perovskite film, and the s-SWNT-added perovskite film exhibit the (110) peaks with the FWHM values of 0.456, 0.469, and 0.448, respectively (Fig S12, Table S4). Therefore, the crystal grain size of the water-added perovskite films is the smallest and that of the s-SWNT-added perovskite films is the largest, which agree with the observation made from the AFM images in Figure 2. In addition, the intensity ratio of the (110) peak to the (220) peak indicates the growth of the (110)-oriented grains,[47,48] which is favourable for the hole injection from the perovskite to spiro-MeOTAD.[49] The s-SWNT-added films exhibit the greatest ratio of 1.58 (Table S4). The XRD spectra with varying s-SWNT$_{(aq)}$ concentrations show that the grain size increases with the increase in the amount of s-SWNTs added (Fig. S13 and S14, Table S5). The small peak at 13.0° comes from the lattice planes of hexagonal PbI_2.[50] The peak is suppressed with the increase in the s-SWNT$_{(aq)}$ concentration, indicating that the hydrophobic s-SWNTs at the grain boundaries might be protecting the perovskite films from environmental degradation or dissociation (Fig. S13b). The existence of PbI_2 in perovskite film is known to increase J_{SC} and FF, but decrease V_{OC}. If PbI_2 is deficient, the opposite effect will take place. This indicates that the small amount of PbI_2 might have contributed to the high V_{OC} obtained from the s-SWNT-added devices (Fig. S6, Table 1). Trap-states at the grain boundaries induce non-radiative recombination, decreasing the charge carrier lifetime and broadening photoluminescence (PL) peak.[16,51,52,53] While both the water-added and the s-SWNT-added perovskite films exhibited blue shifts compared with the reference films, the s-SWNT-added perovskite films displayed marginally smaller FWHM, indicating possible passivation of the trap states by DOCs on SWNTs (Fig. S15).[8,54] Transient PL substantiates this by revealing that the s-SWNT-added perovskite films show longer average carrier lifetime (Fig. S16). Further evidence for the trap sites passivation can be found from the XPS data in Figure 3b.[55] Both the water-added perovskite films and the s-SWNTs-added perovskite films have the Pb $4f_{5/2}$ and $4f_{7/2}$ peaks shifted to a higher binding energy compared with those of the reference films. The shifts are due to the perovskite crystals containing less metallic Pb, which proves the higher quality of the perovskite films.[56,57,58] Notably, the peaks of the s-SWNTs-added perovskite films are narrower than the other films, because there are less Pb^{2+} species owing to the greater grain size and the passivation from the s-SWNTs. PSCs with DOCs as additives without s-SWNTs were fabricated. The devices exhibited significantly low PCEs with notably high series resistance (R_S) values (Table S6). This shows that DOCs alone cannot function as the charge transporters and s-SWNT backbones are necessary as they enhance the charge flow of the perovskite film (Fig. S17). Furthermore, conductive-AFM of the s-SWNT-added perovskite films show more highly conductive spots at the grain boundaries than the water-added perovskite films, corroborating the charge conductivity enhancement with

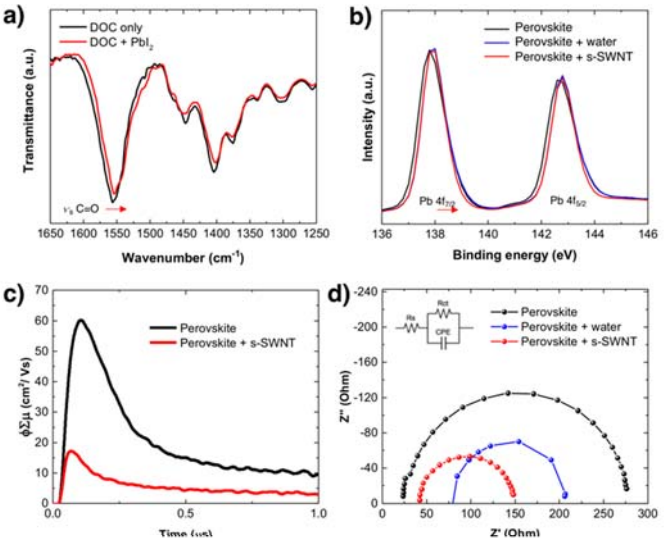

Fig .3 (a) FTIR spectra of DOC pellet (black) and DOC pellet containing PbI2 (red). (b) Pb 4f7/2 and Pb 4f5/2 peaks of the XPS spectra of the MAPbI3 film (black), the water-added MAPbI3 film (blue), and the s-SWNT-added MAPbI3 film (red). (c) The yield of free charge carriers (Φ) multiplied by the sum of the carrier mobilities (Σμ = μe + μh) giving the yield-mobility product (ΦΣμ) over time for the MAPbI3 film (black) and the s-SWNT-added MAPbI3 film (red) with the spiro-MeOTAD coated on top. (d) Nyquist plots of MAPbI3 film (black), the water-added MAPbI3 film (blue), and the s-SWNT-added MAPbI3 film (red) obtained from the impedance measurement.

the presence of s-SWNTs (Fig. S18). Time-resolved microwave conductivity (TRMC) measurement shows that the perovskite films with s-SWNTs exhibit much faster decay, suggesting improved charge extraction kinetics (mainly holes) from the perovskite active layer to the spiro-MeOTAD layer (Fig. 3c).[30,59] This is related to the aforementioned enhancement of film hole mobility and (110)-oriented grains. To gain further insight into the roles of s-SWNT in the perovskite film, the electrical impedance spectroscopy (EIS) analysis was conducted. Figure 3d shows the Nyquist plots of the reference perovskite film, the water-added perovskite film, and the s-SWNT-added perovskite films under illumination, with the equivalent circuit shown in the inset. It is known that in the EIS analysis, the high frequency component represents the charge transfer resistance (R_{ct}).[60] In the present study, the only variable affecting R_{ct} is the additives in perovskite films. The numerical fitting of EIS data gives the parameters as listed in Table S7. Obviously, compared with the R_{ct} of 248.3 Ω from the reference sample, the water-added and s-SWNT-added samples show smaller R_{ct} of 121.2 Ω and 95.8 Ω, respectively. The smaller R_{ct} implies more efficient charge extraction from the perovskite active layer, which can arise from the improved morphology and coverage of perovskite film due to the water additive. Furthermore, even smaller R_{ct} of 95.8 Ω upon addition of s-SWNTs due to more efficient charge extraction by passivation of the grain boundaries and reduced trap sites. As complementary experiments, we tested PSCs with pure metallic single-walled carbon nanotubes rather than semiconducting carbon nanotubes. PSCs with metallic single-walled carbon nanotubes exhibited poor PCEs with extremely low R_{SH}, indicating the importance of s-SWNT purity (Table S8). It is worth noting that the addition of s-SWNTs did not manifest any significant change in the device stability.[61] We conjecture

that this is due to the s-SWNT added being too small to have a noticeable effect.

Conclusion

By incorporating a small amount of s-SWNTs in deionised water, a PSC PCE of 18.1% increased to 19.5%. The added s-SWNTs worked as both crystal growth templates and grain boundary passivators thanks to the attached DOC surfactants. The s-SWNTs themselves functioned as charge bridges at the grain boundaries as well, increasing the mobility of the perovskite film. The resulting effects were increased grain size and reduced charge trap, which were reflected by the increased J_{SC} and V_{OC}. The FF improvement was limited in comparison with the water-added control devices, which, we predict, can be resolved by using purer s-SWNTs and surfactants with higher mobility than DOC. As the technology of this work does not require a large amount of s-SWNTs which are costly, the potential feasibility of this work can be said to be excellent. Therefore, we expect further follow-ups of this work in near future.

Conflicts of interest

There are no conflicts to declare.

Acknowledgements

We gratefully acknowledge the Research and Education Consortium for Innovation of Advanced Integrated Science by Japan Science and Technology (JST) and Japan Society for the Promotion of Science JSPS KAKENHI Grant Numbers JP15H05760, JP16H02285, JP17K04970, JP17H06609, JP18H05329 and 19K15669. I.J. thanks Yashima foundation for financial support.

Author Contribution

S.S. and I.J. contributed equally to this work. S.S., I.J. Y.M. and S.M. conceived and designed the project. S.S. performed device fabrications. X.R. conducted TEM. T.O. performed the PL measurement. I.J. and D.S. performed the FTIR measurement. C. L. and H. M. L. performed the DFT calculation. J.-W.L. performed the c-AFM measurement. R.N. and A.S. performed TRMC experiments. H.Z., T.T. and H.K. performed separation of s-SWNT. S.S. and I.J. wrote the manuscript. S.C., J.S. and Y.Y. assisted with the interpretation of the data. I.J., Y.M. and S.M. supervised the project. All of authors discussed the results and commented on the manuscript.

References

1 A. Kojima, K. Teshima, Y. Shirai, T. Miyasaka, *J. Am. Chem. Soc.*, 2009, **131**, 6050–6051.
2 W. S. Yang, B.-W. Park, E. H. Jung, N. J. Jeon, Y. C. Kim, D. U. Lee, S. S. Shin, J. Seo, E. K. Kim, J. H. Noh, S. I. Seok, *Science*, 2017, **356**, 1376–1379.
3 H.-S. Kim, C.-R. Lee, J.-H. Im, K.-B. Lee, T. Moehl, A. Marchioro, S.-J. Moon, R. Humphry-Baker, J.-H. Yum, J. E. Moser, M. Gratzel, *Sci. Rep.,* 2012, **2**, 591.
4 M. M. Lee, J. Teuscher, T. Miyasaka, T. N. Murakami, H. J. Snaith, *Science*, 2012, **338**, 643–647.
5 J.-W. Lee, D.-J. Seol, A.-N. Cho, N.-G. Park, *Adv. Mater.*, 2014, **26**, 4991–4998.
6 G. Xing, N. Mathews, S. Sun, S. S. Lim, Y. M. Lam, M. Gratzel, S. Mhaisalkar, T. C. Sum, *Science*, 2013, **342**, 344–347.
7 W.-J. Yin, T. Shi, Y. Yan, *Appl. Phys. Lett.*, 2014, **104**, 063903.
8 D. W. de Quilettes, S. M. Vorpahl, S. D. Stranks, H. Nagaoka, G. E. Eperon, M. E. Ziffer, H. J. Snaith, D. S. Ginger, *Science*, 2015, **348**, 683–686.
9 S. Y. Leblebici, L. Leppert, Y. Li, S. E. Reyes-Lillo, S. Wickenburg, E. Wong, J. Lee, M. Melli, D. Ziegler, D. K. Angell, D. F. Ogletree, P. D. Ashby, F. M. Toma, J. B. Neaton, I. D. Sharp, A. W.-Bargioni, *Nat. Energy*, 2016, **1**, 16093.
10 Y. Kutes, Y. Zhou, J. L. Bosse, J. Steffes, N. P. Padture, B. D. Huey, *Nano Lett.*, 2016, **16**, 3434–3441.
11 G. E. Eperon, S. D. Stranks, C. Menelaou, M. B. Johnston, L. M. Herz, H. J. Snaith, *Energy Environ. Sci.*, 2014, **7**, 982.
12 N. J. Jeon, J. H. Noh, Y. C. Kim, W. S. Yang, S. Ryu, S. Il. Seok, Nat. Mater., 2014, **13**, 897–903.
13 Y. Tidhar, E. Edri, H. Weissman, D. Zohar, G. Hodes, D. Cahen, B. Rybtchinski, S. Kirmayer, *J. Am. Chem. Soc.*, 2014, **136**, 13249–13256.
14 D. Bi, C. Yi, J. Luo, J. Décoppet, F. Zhang, S. M. Zakeeruddin, X. Li, A. Hagfeldt, M. Grätzel, *Nat. Energy,* 2016, **1**, 16142.
15 J. Peng, J. I. Khan, W. Liu, E. Ugur, T. Duong, Y. Wu, H. Shen, K. Wang, H. Dang, E. Aydin, X. Yang, Y. Wan, K. J. Weber, K. R. Catchpole, F. Laquai, S. D. Wolf, T. P. White., *Adv. Energy Mater.,* 2018, **8**, 1801208.
16 D. Bi, W. Tress, M. I. Dar, P. Gao, J. Luo, C. Renevier, K. Schenk, A. Abate, F. Giordano, J.-P. Correa Baena, J.-D. Decoppet, S. M. Zakeeruddin, M. K. Nazeeruddin, M. Gratzel, A. Hagfeldt, *Sci. Adv.*, 2016, **2**, e1501170–e1501170.
17 W.-J. Yin, T. Shi, Y. Yan, *Adv. Mater.*, 2014, **26**, 4653–4658.
18 C. G. Bischak, E. M. Sanehira, J. T. Precht, J. M. Luther, N. S. Ginsberg, *Nano Lett.*, 2015, **15**, 4799–4807.
19 J.-W. Lee, S.-H. Bae, Y.-T. Hsieh, N. De Marco, M. Wang, P. Sun, Y. Yang, *Chem*, 2017, **3**, 290–302.
20 R. Brenes, D. Guo, A. Osherov, N. K. Noel, C. Eames, E. M. Hutter, S. K. Pathak, F. Niroui, R. H. Friend, M. S. Islam, H. J. Snaith, V. Bulovic, T. J. Savenije, S. D. Stranks, *Joule*, 2017, **1**, 155–167.
21 W. Zhang, S. Pathak, N. Sakai, T. Stergiopoulos, P. K. Nayak, N. K. Noel, A. A. Haghighirad, V. M. Burlakov, D. W. DeQuilettes, A. Sadhanala, W. Li, L. Wang, D. S. Ginger, R. H. Friend, H. J. Snaith, *Nat. Commun.*, 2015, **6**, 10030.
22 M. Yang, Y. Zhou, Y., Zeng, C.-S. Jiang, N. P. Padture, K. Zhu, *Adv. Mater.,* 2015, **27**, 6363–6370.
23 Y. Chen, B. Li, W. Huang, D. Gao, Z. Liang, *Chem. Commun.,* 2015, **51**, 11997–11999.
24 S. Berson, R. de Bettignies, S. Bailly, S. Guillerez, B. Jousselme, P. Cells, B. S. Berson, R. De Bettignies, S. Bailly, S. Guillerez, B. Jousselme, *Adv. Funct. Mater.,* 2007, **17**, 3363–3370.
25 S. Chaudhary, H. Lu, A. M. Müller, C. J. Bardeen, M. Ozkan, *Nano Lett.*, 2007, **7**, 1973–1979.
26 I. Jeon, D. Kutsuzawa, Y. Hashimoto, T. Yanase, T. Nagahama, T. Shimada, Y. Matsuo, *Org. Electron.*, 2015, **17**, 275–280.
27 Y. Wu, X. Yang, W. Chen, Y. Yue, M. Cai, F. Xie, E. Bi, A. Islam, L. Han, *Nat. Energy*, 2016, **1**, 16148.
28 C.-H. Chiang, C.-G. Wu, *Nat. Photonics*, 2016, **10**, 196–200.
29 N. Ahn, I. Jeon, J. Yoon, E. I. Kauppinen, Y. Matsuo, S. Maruyama, M. Choi, *J. Mater. Chem. A*, 2018, **6**, 1382–1389.
30 R. Ihly, A.-M. Dowgiallo, M. Yang, P. Schulz, N. J. Stanton, O. G. Reid, A. J. Ferguson, K. Zhu, J. J. Berry, J. L. Blackburn, *Energy Environ. Sci.*, 2016, **9**, 1439–1449.
31 Y. Zhang, L. Tan, Q. Fu, L. Chen, T. Ji, X. Hu, Y. Chen, *Chem. Commun.,* 2016, **52**, 5674–5677.

32 M. S. Fuhrer, J. Nygard, L. Shih, M. Forero, Y. Yoon, M. S. C. Mazzoni, H. J. Choi, J. Ihm, S.G. Louie, A. Zettl, P. L. McEuen, *Science,* 2000, **288**, 494–497.
33 P. N. Nirmalraj, P. E. Lyons, S. De, J. N. Coleman, J. J. Boland, *Nano Lett*., 2009, **9**, 3890–3895.
34 C.-G. Wu, C.-H. Chiang, Z.-L. Tseng, M. K. Nazeeruddin, A. Hagfeldt, M. Grätzel, *Energy Environ. Sci.,* 2015, **8**, 2725–2733.
35 X. Gong, M. Li, X.-B. Shi, H. Ma, Z.-K. Wang, L.-S. Liao, *Adv. Funct. Mater.*, 2015, **25**, 6671–6678.
36 D. Liu, C. J. Traverse, P. Chen, M. Elinski, C. Yang, L. Wang, M. Young, R. R. Lunt, *Adv. Sci.,* 2018, **5**, 1700484.
37 C.-H. Chiang, M. K. Nazeeruddin, M. Grätzel, C.-G. Wu, *Energy Environ. Sci.,* 2017, **10**, 808–817.
38 B. Conings, A. Babayigit, T. Vangerven, J. D'Haen, J. Manca, H.-G. Boyen, *J. Mater. Chem. A*, 2015, **3**, 19123–19128.
39 N. Adhikari, A. Dubey, E. A. Gaml, B. Vaagensmith, K. M. Reza, S. A. A. Mabrouk, S. Gu, J. Zai, X. Qian, Q. Qiao, *Nanoscale*, 2016, **8**, 2693–2703.
40 Y. Guo, K. Shoyama, W. Sato, E. Nakamura, *Adv. Energy Mater.* 2016, **6**, 1502317.
41 N. Ahn, D.-Y. Son, I.-H. Jang, S. M. Kang, M. Choi, N. Park, *J. Am. Chem. Soc.*, 2015, **137**, 8696–8699.
42 F. Li, H. Wang, D. Kufer, L. Liang, W. Yu, E. Alarousu, C. Ma, Y. Li, Z. Liu, C. Liu, N. Wei, F. Wang, L. Chen, O. F. Mohammed, A. Fratalocchi, X. Liu, G. Konstantatos, T. Wu, *Adv. Mater.*, 2017, **29**, 1602432.
43 I. Ka, L. F. Gerlein, R. Nechache, S. G. Cloutier, *Sci. Rep.*, 2017, **7**, 45543.
44 F. Cui, *Int. J. Nanomedicine*, 2011, **6**, 3049.
45 J.-W. Lee, H.-S. Kim, N.-G. Park, *Acc. Chem. Res.*, 2016, **49**, 311–319.
46 B. D. Hall, D. Zanchet, D. Ugarte, *J. Appl. Crystallogr.,* 2000, **33**, 1335–1341.
47 Q. Wang, M. Lyu, M. Zhang, J.-H. Yun, H. Chen, L. Wang, *J. Phys. Chem. Lett.,* 2015, **6**, 4379–4384.
48 Z. Li, C. Kolodziej, C. McCleese, L. Wang, A. Kovalsky, A. C. Samia, Y. Zhao, C. Burda, *Nanoscale Adv.*, 2019, **1**, 827–833.
49 J. Yin, D. Cortecchia, A. Krishna, S. Chen, N. Mathews, A. C. Grimsdale, C. Soci, *J. Phys. Chem. Lett.,* 2015, **6**, 1396–1402.
50 T. Zhang, N. Guo, G. Li, X. Qian, Y. Zhao, *Nano Energy*, 2016, **26**, 50–56.
51 W. Nie, H. Tsai, R. Asadpour, J.-C. Blancon, A. J. Neukirch, G. Gupta, J. J. Crochet, M. Chhowalla, S. Tretiak, M. A. Alam, H.-L. Wang, A. D. Mohite, *Science*, 2015, **347**, 522–525.
52 P. Zhao, B. J. Kim, H. S. Jung, *Mater. Today Energy*, 2018, **7**, 267–286.
53 M.-H. Park, S.-H. Jeong, H.-K. Seo, C. Wolf, Y.-H. Kim, H. Kim, J. Byun, J. S. Kim, H. Cho, T.-W. Lee, *Nano Energy*, 2017, **42**, 157-165.
54 Z. Chu, M. Yang, P. Schulz, D. Wu, X. Ma, E. Seifert, L. Sun, X. Li, K. Zhu, K. Lai, *Nat. Commun.,* 2017, **8**, 2230.
55 I. Jeon, S. Zeljkovic, K. Kondo, M. Yoshizawa, Y. Matsuo, *ACS Appl. Mater. Interfaces*, 2016, **8**, 29866–29871.
56 R. Lindblad, D. Bi, B. Park, J. Oscarsson, M. Gorgoi, H. Siegbahn, M. Odelius, E. M. J. Johansson, H. Rensmo, *J. Phys. Chem. Lett.,* 2014, **5**, 648–653.
57 H. Cho, S.-H. Jeong, M.-H. Park, Y.-H. Kim, C. Wolf, C.-L. Lee, J. H. Heo, A. Sadhanala, N. Myoung, S. Yoo, S. H. I., R. H. F., T.-W. Lee, *Science*, 2015, **350**, 1222–1225.
58 Q. Dong, Y. Fang, Y. Shao, P. Mulligan, J. Qiu, L. Cao, J. Huang, *Science*, 2015, **347**, 967–970.
59 K. Wojciechowski, S. D. Stranks, A. Abate, G. Sadoughi, A. Sadhanala, N. Kopidakis, G. Rumbles, C. Z. Li, R. H. Friend, A. K. Y. Jen, H. J. Snaith, *ACS Nano,* 2014, **8**, 12701–12709.
60 D. Yang, R. Yang, J. Zhang, Z. Yang, S. (Frank) Liu, C. Li, *Energy Environ. Sci.,* 2015, **8**, 3208–3214.
61 M. Batmunkh, C. J. Shearer, M. Bat-Erdene, M. J. Biggs, J. G. Shapter, ACS Appl. Mater. Interfaces, 2017, **9**, 19945–19954.

Table 1 Photovoltaic parameters of the reference PSCs and the PSCs using water and s-SWNT$_{(aq)}$ as additives under 1 sun (AM 1.5 G, 100 mW cm-2), showing the best and average PCE values.

Active Layer	J_{SC} (mA cm^{-2})	V_{OC} (V)	FF	R_S (Ω cm^2)	R_{SH} (Ω cm^2)	PCE$_{best}$	PCE$_{average}$
$MAPbI_3$	23.1	1.06	0.74	29.7	$4.53x10^4$	18.1%	17.1±0.9%
$MAPbI_3$ + 2wt% water	22.9	1.08	0.76	58.5	$1.94x10^5$	18.7%	18.3±0.5%
$MAPbI_3$ + 2wt% s-SWNT$_{(aq)}$	23.7	1.14	0.72	92.6	$8.87x10^4$	19.5%	18.9±0.5%

Table 2 Photovoltaic performance of the s-SWNT-added PSCs with varying s-SWNT$_{(aq)}$ concentrations under 1 sun (AM 1.5 G, 100 mW cm^{-2}).

s-SWNT concentration	J_{SC} (mA cm^{-2})	V_{OC} (V)	FF	R_S (Ω cm^2)	R_{SH} (Ω cm^2)	PCE$_{best}$ (%)	PCE$_{average}$ (%)
1wt%	23.5	1.08	0.76	45.6	$5.69x10^4$	19.3	18.7 ±0.5
2wt%	23.7	1.14	0.72	72.6	$1.87x10^4$	19.5	19.1 ±0.3
3wt%	22.4	1.13	0.70	84.4	$7.95x10^4$	18.2	18.0 ±0.2
10wt%	20.5	1.15	0.68	93.5	$2.28x10^4$	15.4	14.5 ±0.8

Electronic Supporting Information (ESI)

Semiconducting Carbon Nanotubes as Crystal Growth Templates and Grain Bridges in Perovskite Solar Cells

Seungju Seo,‡[a] Il Jeon,‡[a] Rong Xiang,[a] Changsoo Lee,[b] Hao Zhang,[a] Takeshi Tanaka,[c] Jin-Wook Lee,[d] Donguk Suh,[a] Tatsuro Ogamoto,[a] Ryosuke Nishikubo,[e] Akinori Saeki,[e] Shohei Chiashi,[a] Junichiro Shiomi,[a] Hiromichi Kataura,[c] Hyuck Mo Lee,[b] Yang Yang,[d] Yutaka Matsuo*[a,f] and Shigeo Maruyama*[a,g]*

AUTHOR ADDRESS

a: Department of Mechanical Engineering, The University of Tokyo, 7-3-1 Hongo, Bunkyo-ku, Tokyo 113-8656, Japan

b**:** Department of Materials Science and Engineering, KAIST, 291 Daehak-ro, Yuseong-gu, Daejeon, 34141, Republic of Korea

c: Nanomaterials Research Institute, National Institute of Advanced Industrial Science and Technology (AIST), Tsukuba, Ibaraki 305-8565, Japan

d: Department of Materials Science and Engineering, University of California, Los Angeles, Los Angeles, CA 90095, USA

e: Department of Applied Chemistry, Osaka University, Osaka, 565-0871 Japan

f: Hefei National Laboratory for Physical Sciences at the Microscale, University of Science and Technology of China, Hefei, Anhui 230026, China

g: Energy NanoEngineering Lab., National Institute of Advanced Industrial Science and Technology (AIST), Tsukuba, Ibaraki 305-8564, Japan

‡ These authors contributed equally.

I.J. E-mail: il.jeon@spc.oxon.org
Y.M. E-mail: matsuo@photon.t.u-tokyo.ac.jp

S.M. E-mail: maruyama@photon.t.u-tokyo.ac.jp

Experimental Section

s-SWNT Dispersion Preparation. Preparation of s-SWNT dispersion was performed according to the literature.[1,2] The SWNTs synthesized by high-pressure carbon monoxide processing (HiPco, raw soot, RO513, NanoIntegris, 1.0 – 0.3 nm in diameter) were used in this study. Dispersions of the SWNTs was prepared by dropping 1 mg mL^{-1} of the as-prepared SWNTs in 1% SDS (99%, Sigma–Aldrich) solution and then ultrasonicating the mixture using a tip-type ultrasonic homogenizer (Sonifire 250D, Branson) for 3 h under cooling at 15 ℃. The solution was then centrifuged to remove bundles and impurities (210,000 x g for 30 min at 25 ℃). The resulting supernatant was collected as a dispersant of surfactant-coated SWNTs. A chromatography system (AKTA, GE Healthcare) equipped with a column packed with agarose gel beads was used for the separation of metallic and semiconducting SWNTs. After equilibration of the column with 1% SDS solution, the SWNT dispersion was applied. Metallic and semiconducting SWNTs were obtained as unbound fraction in 1% SDS and bound fraction eluted by 1% DOC, respectively.

Perovskite Precursor Solution Preparation. For the $MAPbI_3$ Solution, CH_3NH_3I (TCI), PbI_2 (TCI), and anhydrous dimethyl sulfoxide (TCI) (molar ratio 1:1:1) were mixed in anhydrous *N,N*-dimethylformamide (TCI) with a concentration of 50 wt%. The solution was filtered through a 0.45 μm poly(tetrafluoroethylene) filter before use. For the water-added $MAPbI_3$ solution, 2 wt% pure water (Fujifilm Wako Pure Chemical Co.) was added into the prepared $MAPbI_3$ solution. The solution was filtered through a 0.45 μm poly(tetrafluoroethylene) filter before use. For the s-SWNT-added $MAPbI_3$ solution, 2 wt% semiconducting SWNT dispersion was added into the prepared $MAPbI_3$ solution. The solution was filtered through a 0.45 μm poly(tetrafluoroethylene) filter before use.

Perovskite Solar Cell Fabrication. ITO patterned glass substrates were cleaned and sonicated with detergent, distilled water, acetone, and isopropanol in an ultrasonic bath for 15 min, respectively. The cleaned substrates underwent the UV-ozone for enhanced wettability. Thirty millimolar $SnCl_2 \cdot 2H_2O$ (Aldrich, >99.995%) solution was prepared in ethanol (anhydrous, Fujifilm Wako Pure Chemical Co.) as a precursor solution for deposition of a compact SnO_2 layer. The solution was filtered by a 0.2 μm syringe filter, followed by spin-coating on the cleaned substrate at 3000 rpm for 30 s. The spin-coated film was annealed at 150 °C for 30 min. After cooling down to room temperature, another cycle of the spin-coating process was repeated, which was followed by annealing at 150 °C for 5 min and 180 °C for 1 h. The SnO_2-coated ITO glass was treated with UV-ozone before spin-coating of the prepared perovskite solution. Then, 25 μL of perovskite precursor solution was spin-coated onto the SnO_2 layer at 3000 rpm for 30 s, with 0.5 mL of anhydrous diethyl ether slowly dripped onto the substrate 10 s after the start of the spin-coating process. Next, the film was annealed at 100 °C for 10 min to obtain a dense brown $MAPbI_3$ film. The spiro-MeOTAD solution was prepared by dissolving 85.8 mg of spiro-MeOTAD (Merck) in 1 mL of chlorobenzene (anhydrous, 99.8%, Sigma-Aldrich) which was mixed with 33.8 μL of 4-tert-butylpyridine (96%, Aldrich) and 19.3 μL of Li-TFSI (99.95%, Aldrich, 520 mg/mL in acetonitrile) solution. The spiro-MeOTAD solution was spin-coated on the perovskite layer at 3000 rpm for 20 s by dropping 17 μL of the solution during the spinning. Finally, a 70-nm-thick Au anode was fabricated by thermal deposition at a constant evaporation rate of 0.05 nm s^{-1}.

Characterizations. The $J-V$ curves were measured using a software-controlled source meter (Keithley 2400 Source-Meter) under dark conditions and the simulated sunlight irradiation of 1 sun (AM 1.5G; 100 mW cm^{-2}) using a solar simulator (EMS- 35AAA, Ushio Spax Inc.) with an

Ushio Xe short arc lamp 500. The source meter was calibrated using a silicon diode (BS-520BK, Bunkokeiki). The SEM analysis of the perovskite films was performed using an S-4800 (Hitachi). The TEM images are taken by JEM-2010F (JEOL Ltd.) with a thermal field emission gun operated at 200 keV. The selected area electron diffraction (SAED) patterns are recorded by a charge-coupled device at a camera length of 60 cm.

Shimadzu UV-3150 was used for the UV−Vis−NIR measurement. The PL measurement for the chiral mapping and the films were obtained by a home-built micro-PL system with a supercontinuum laser as the excitation (wavelength: 450–2400 nm) and an InGaAs multiarray detector for detecting the emission (900–1600 nm in wavelength). Topography images were recorded by using an atomic force microscope (AFM) operating in tapping mode (SPI3800N, SII). The grazing-incidence XRD 2θ scans were performed on a Jordan Valley D1 diffractometer with a copper Kα1 radiation and a parallel beam source. In the 2θ scans, the scattering angle 2θ between incident beam and diffracted beam changes, whereas the incident angle ω between the incident beam and the sample surface is fixed at 1°. The valence band and the Fermi levels measurements were performed using Riken Keiki PYS-A AC-2 and Kelvin probe spectroscopy in air (ESA), respectively. The photo-emission measurements were performed using XPS (PHI5000, Versa Probe) with monochromatic Al Kα radiation. Fermi levels were measured with a Riken Keiki PYS-A AC-2 photoelectron spectrometer in air. The incident photon-to-current conversion efficiency (IPCE) measurement system consisted of an MLS-1510 monochromator to scan the UV−Vis spectrum. A source measurement unit was used to record the current at each specific wavelength. Two home-made systems based on a Seki Technotron STR-250 laser Raman system (excitation wavelength of 633 nm and 785 nm) and an inVia Raman microscope (Renishaw) were used for Raman measurements. Solartron SI1287 Electrochemical Interface and Solartron 1255B

Frequency Response Analyzer were used for the Impedance Measurement. FT-IR spectra were obtained with a Nicolet Avatar 370 DTGS spectrometer which was fitted with a Smart Performer single-reflection accessory and a flat plate with a ZnSe crystal. For the TRMC measurement, thin film samples were prepared on a quartz plate. The sample was put in a resonant cavity and probed by continuous microwaves at *ca.* 9.1 GHz. The laser excitation from an optical parametric oscillator (OPO, Continuum, Panther) seeded by third-harmonic generation of a Nd:YAG laser (Continuum, Surelite II, 5−8 ns pulse duration, 10 Hz) was set at 500 nm. The photon density (I_0) varied from 1.28×10^{11} to 6.42×10^{14} photons cm^{-2} $pulse^{-1}$. The photoconductivity transient $\Delta\sigma$ was converted to the product of the quantum efficiency of the charge-carrier generation at the pulse end (φ) and the sum of the charge carrier mobilities, $\Sigma\mu$ ($=\mu^{+}+\mu^{-}$), by $\varphi\Sigma\mu = \Delta\sigma(eI_0F_{\mathrm{Light}})^{-1}$, where e and F_{Light} are the unit charge of a single electron and a correction (or filling) factor, respectively.

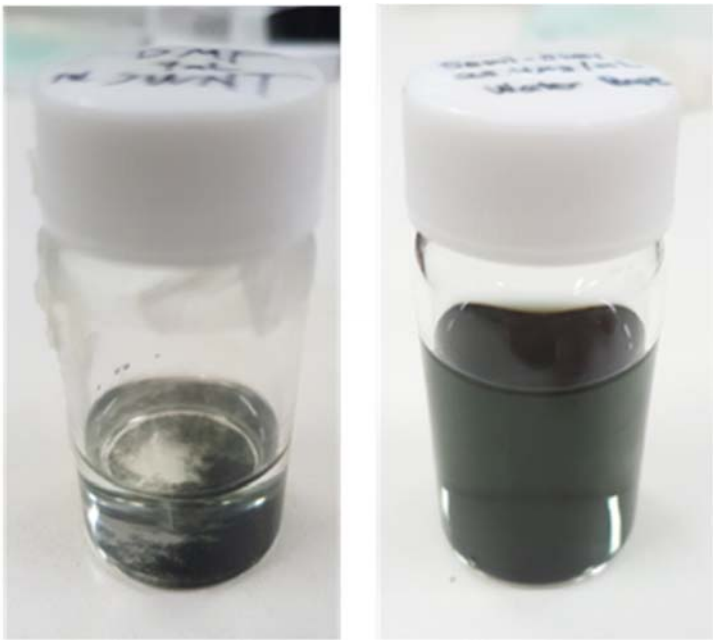

Figure S1. Pictures of SWNTs without surfactants in water (left) and our s-SWNTs with DOCs dispersed in water (right).

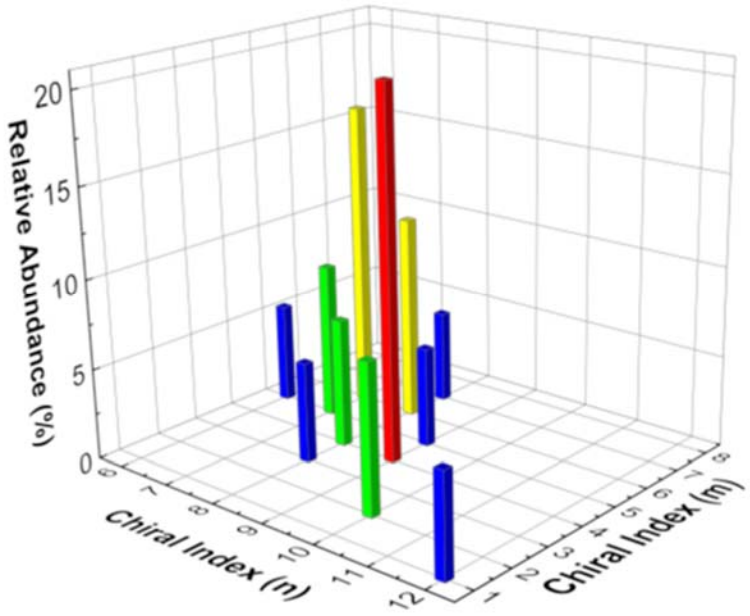

Figure S2. A 3D graph indicating the relative abundance and chirality index (n,m) of s-SWNTs we purified.

Table S1. Chirality mapping table of the s-SWNT solution we purified.

(n,m) index	Diameter (nm)	Chiral angle (θ°)	E11 (nm)	E22 (nm)	PL Intensity (counts)	Relative Abundance (%)
(6,5)	0.76	27.00	983	570	5883	5.53
(7,5)	0.83	24.50	1022	638	9183	8.63
(7,6)	0.90	27.46	1113	642	18060	16.98
(8,3)	0.78	15.30	952	663	5875	5.52
(8,4)	0.84	19.11	1102	578	7523	7.07
(8,6)	0.97	25.28	1165	718	12026	11.31
(8,7)	1.03	27.80	1263	726	5453	5.13
(9,4)	0.92	17.48	1101	720	21780	20.48
(9,5)	0.98	20.63	1244	671	5862	5.51
(10,2)	0.88	8.948	1053	734	8731	8.21
(12,1)	0.99	3.963	1171	797	5978	5.62

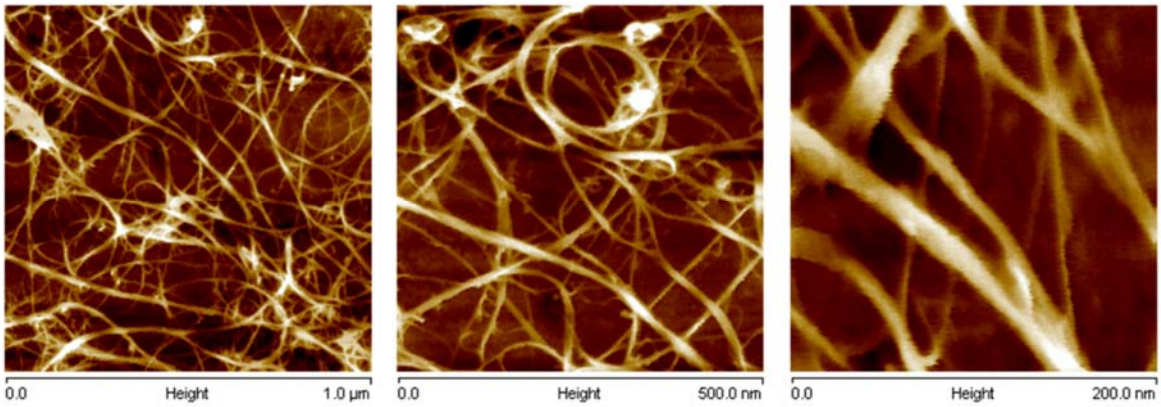

Figure S3. AFM images of the drop-casted s-SWNTs on glass substrates.

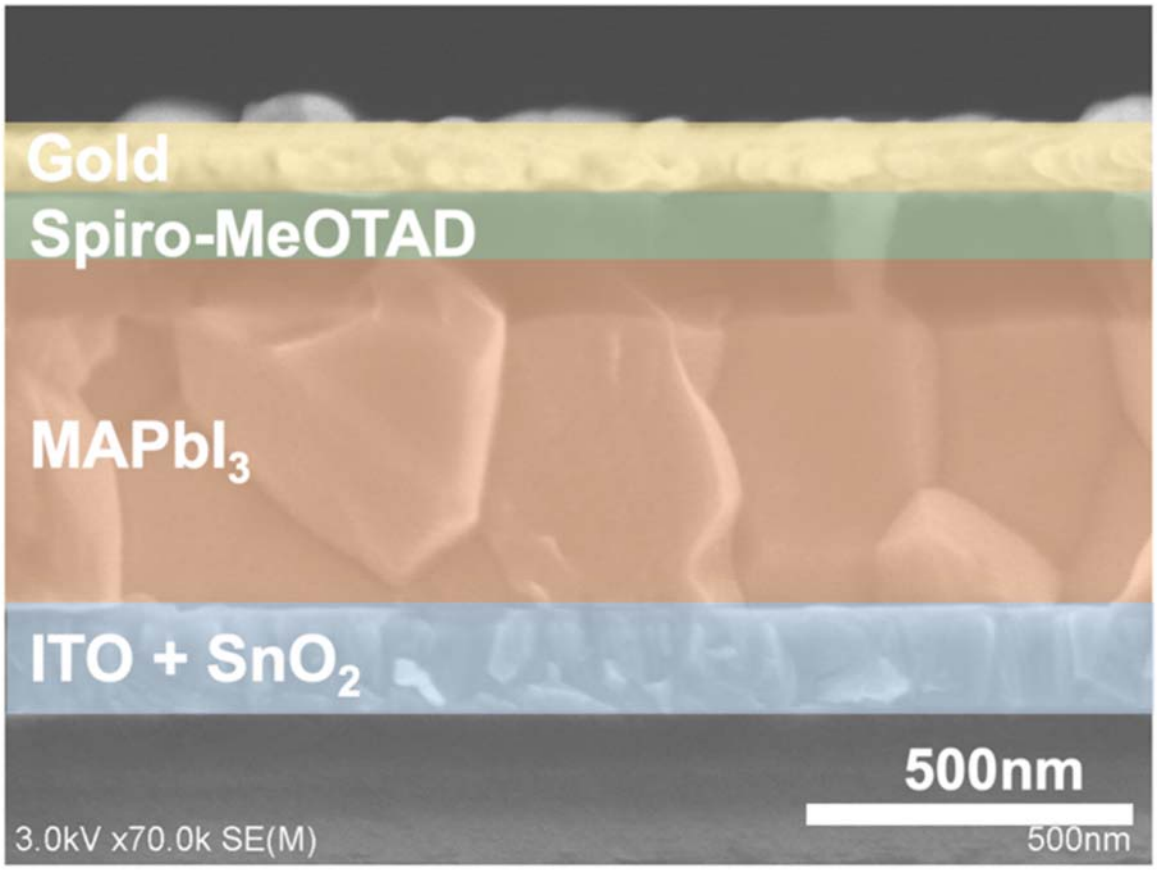

Figure S4. Cross-sectional SEM images of the fabricated PSCs.

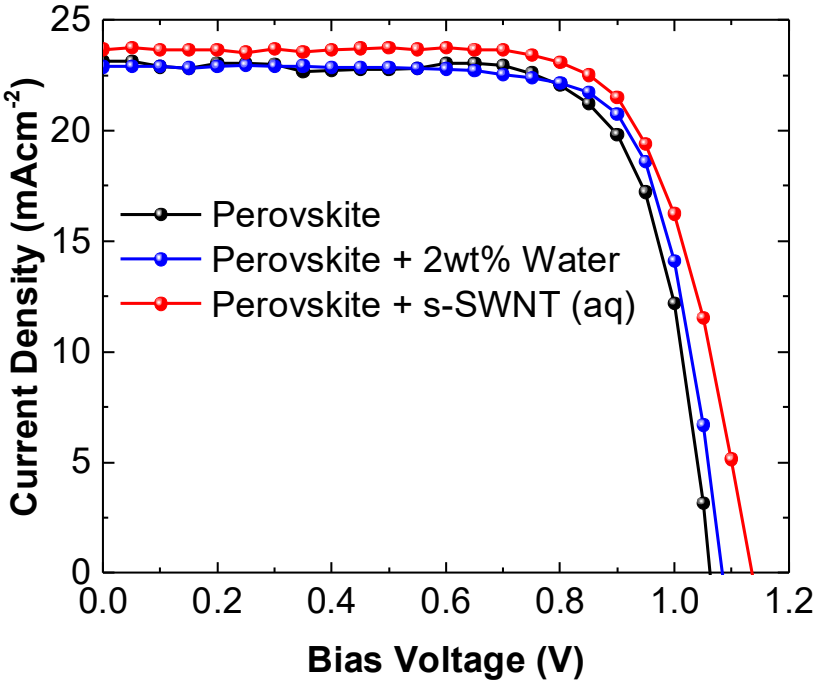

Figure S5. Current density–bias voltage (*J*–*V*) curves of the reference device (black), the water-added PSC (blue), and the s-SWNT-added PSC (red).

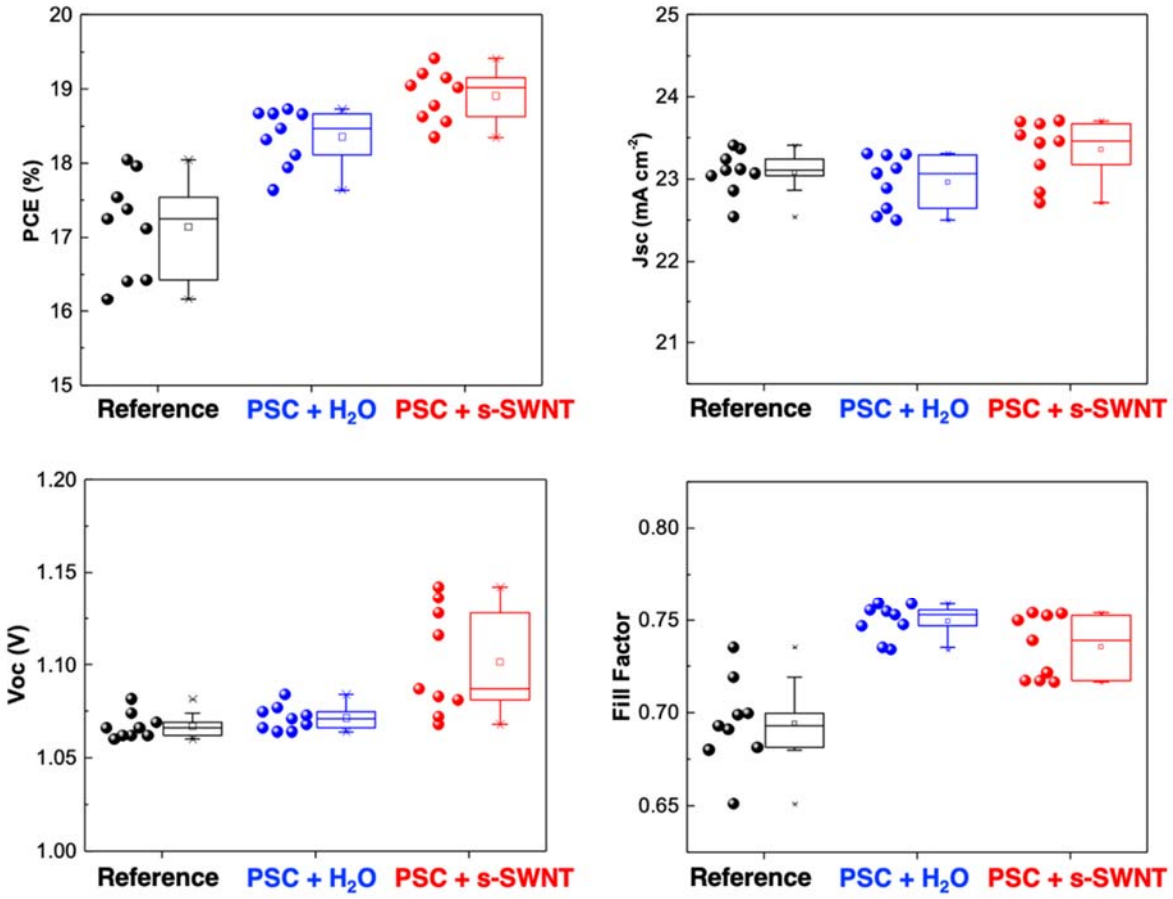

Figure S6. Statistical analyses of the photovoltaic parameters of the reference devices (black), the water-added PSCs (blue), and the s-SWNT-added PSCs (red).

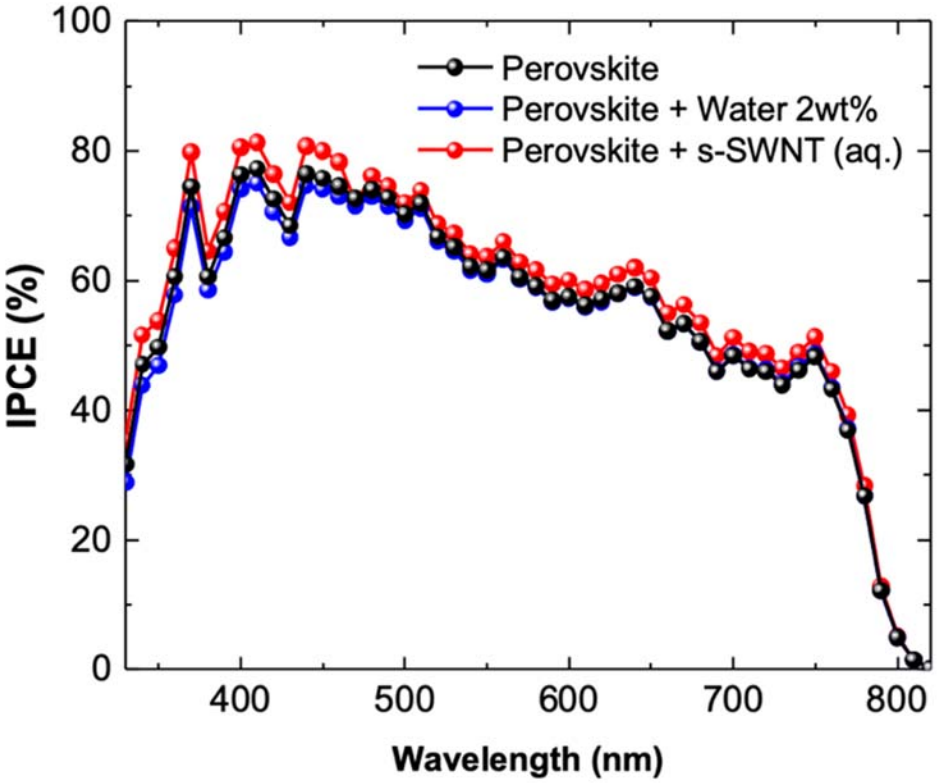

Figure S7. IPCE data of the reference devices (black), the water-added PSCs (blue), and the s-SWNT-added PSCs (red).

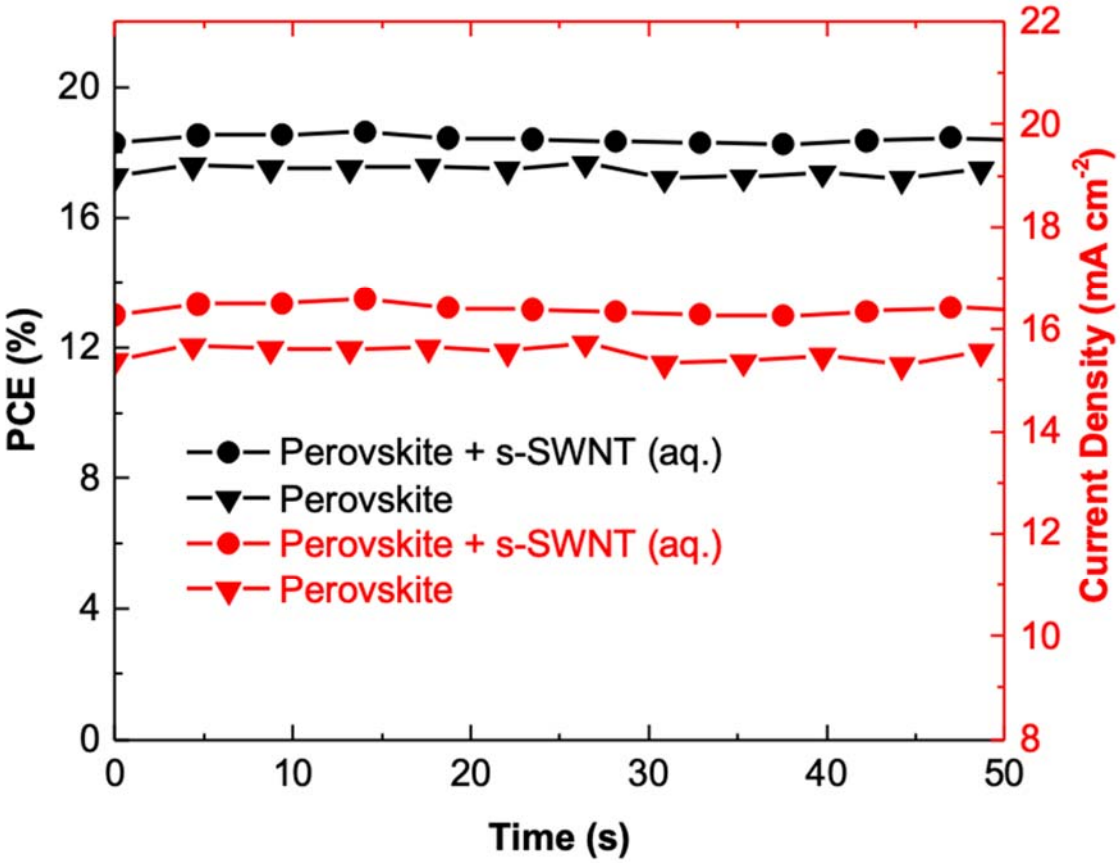

Figure S8. Maximum power point tracking of the reference devices and the s-SWNT-added PSCs.

Table S2. Photovoltaic performance of the water-added PSCs with varying water concentrations.

Water additive concentration	J_{SC} (mA cm^{-2})	V_{OC} (V)	FF	R_S (Ω cm^2)	R_{SH} (Ω cm^2)	PCE_{best} (%)	$PCE_{average}$ (%)
1wt%	23.1	1.06	0.74	51.1	1.15×10^4	18.2	17.9 ±0.3
2wt%	22.9	1.08	0.76	58.5	1.94×10^5	18.7	18.3 ±0.4
3wt%	21.8	1.07	0.75	43.2	5.64×10^5	17.5	17.2 ±0.3
5wt%	22.8	1.10	0.74	63.1	2.46×10^5	18.3	18.1 ±0.4
10wt%	22.4	1.09	0.73	70.9	2.95×10^5	17.9	17.3 ±0.4

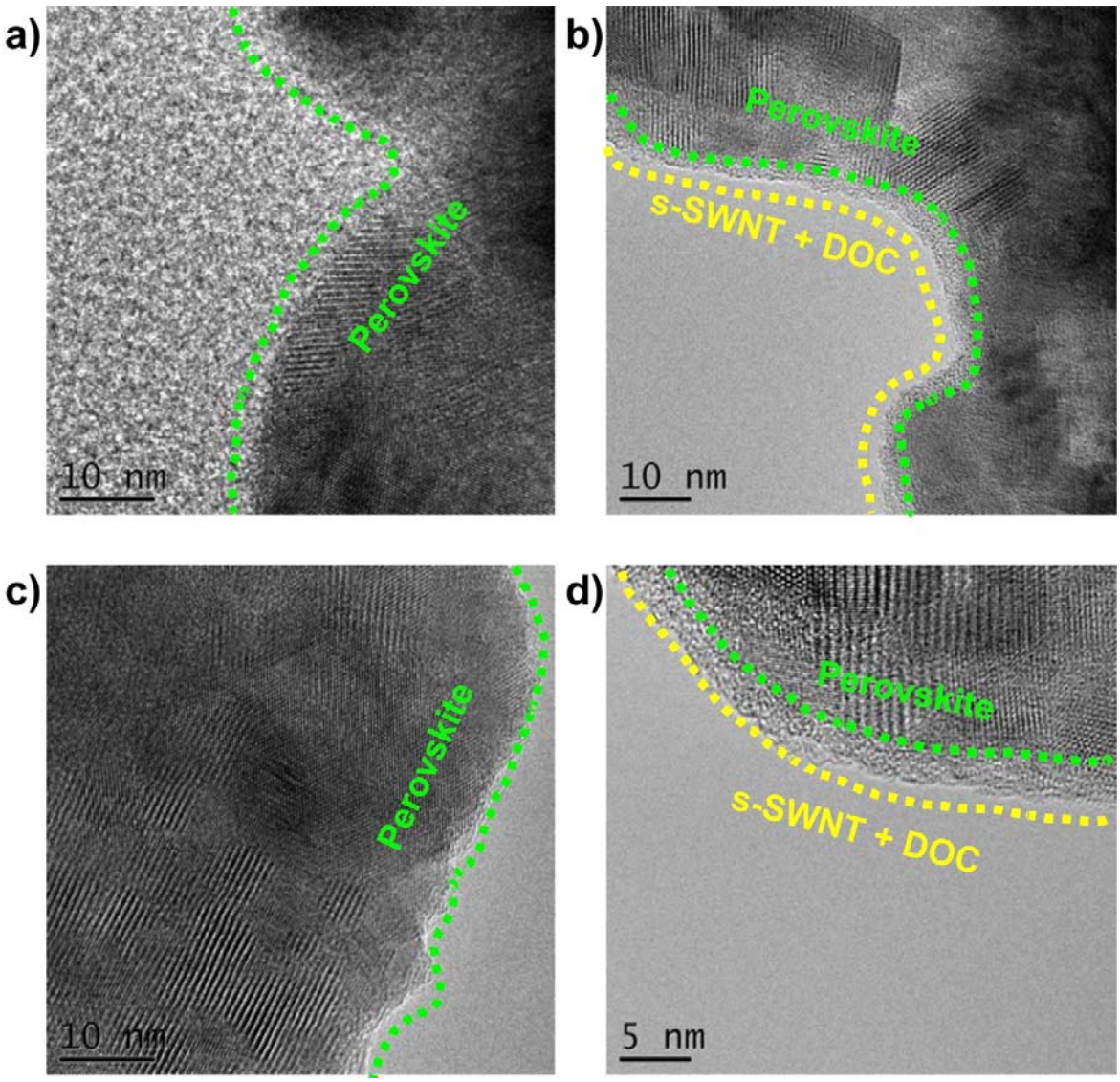

Figure S9. TEM images of (a), (c) the reference perovskite films and (b), (d) the s-SWNT-added perovskite films.

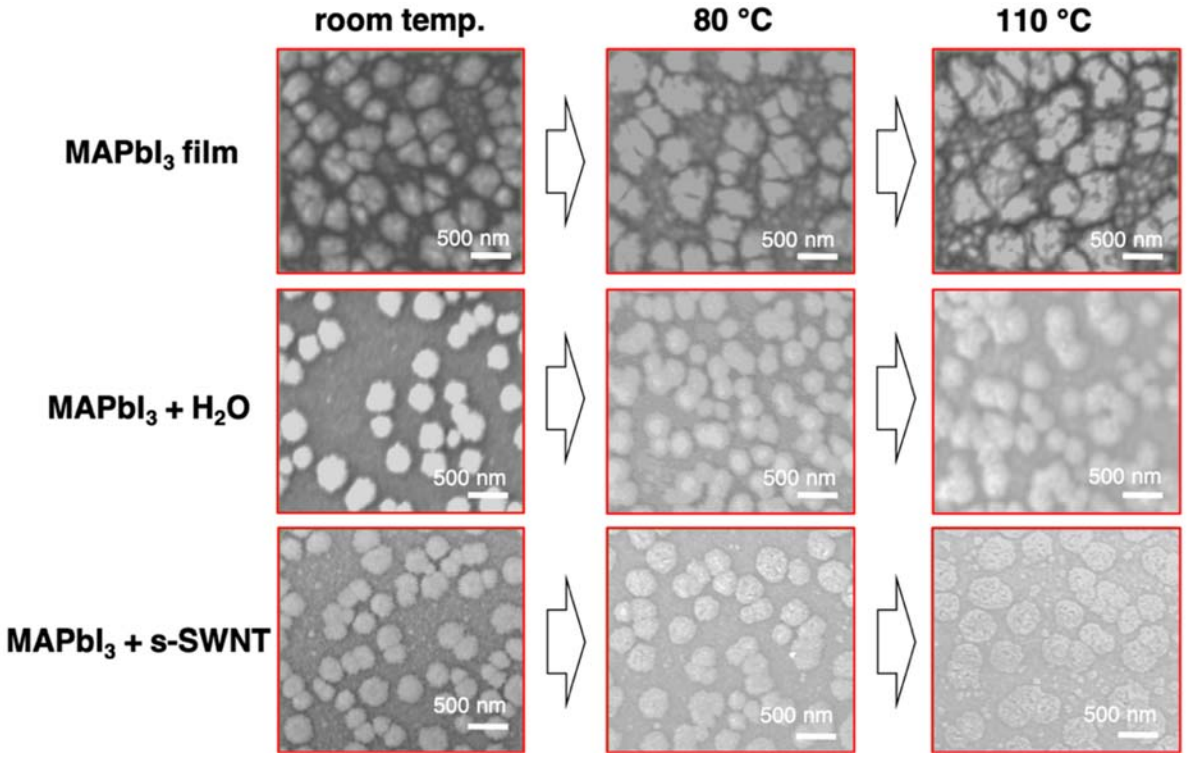

Figure S10. ESEM images of the reference $MAPbI_3$ films, the water-added $MAPbI_3$ films, and the s-SWNT-added $MAPbI_3$ films as we anneal the environmental temperature *in situ*.

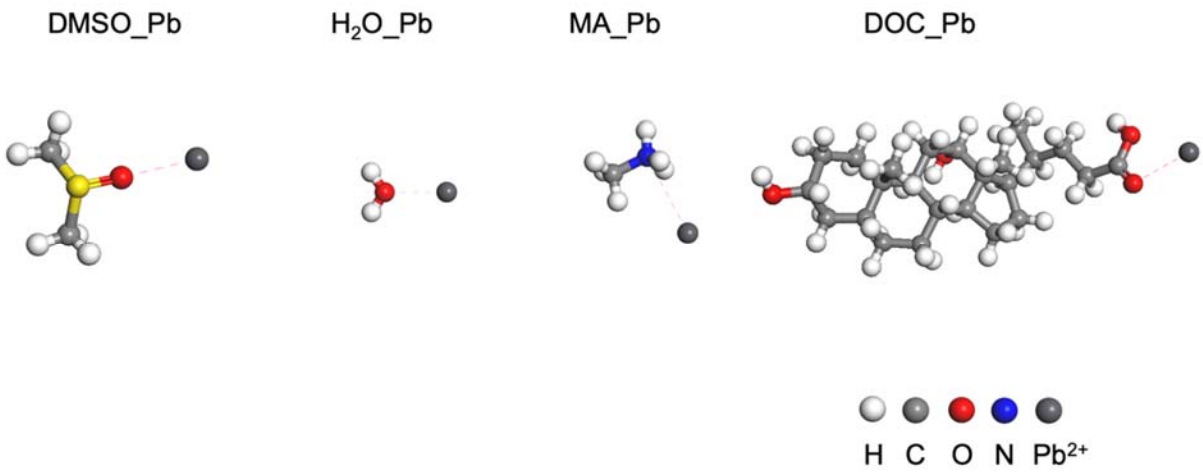

Figure S11. DFT calculation modelling of interaction between Pb^{2+} and the Lewis donors.

Table S3. DFT calculation of interaction between Pb^{2+} and the Lewis donors.

	DMSO	H_2O	MA	DOC
Energy	-50.2	-14.2	-37.1	-392
Energy next to Pb^{2+}	-51.3	-15.2	-39.1	-393
Interaction energy (eV)	-0.506	-0.388	-1.331	-0.525

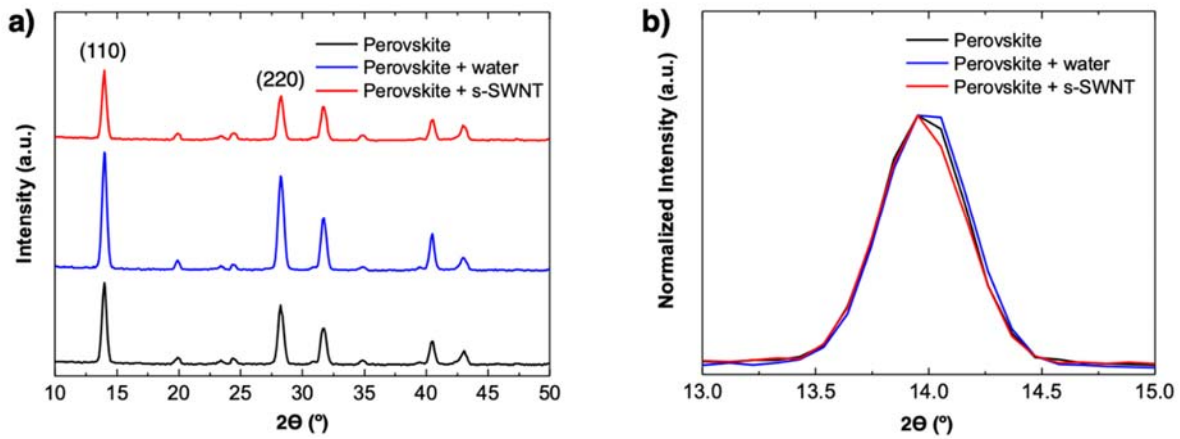

Figure S12. (a) XRD spectra of the reference $MAPbI_3$ films (black), the water-added $MAPbI_3$ films (red), and the s-SWNT-added $MAPbI_3$ films (blue). (b) Normalized (110) peak showing the FWHM trend.

Table S4. XRD peak characterizations and information for the reference $MAPbI_3$ films, the water-added $MAPbI_3$ films, and the s-SWNT-added $MAPbI_3$ films.

Sample	Peak	Position (°)	Intensity	Peak Area	FWHM	Peak Ratio
Perovskite (ref.)	<110>	14.0	1242.87	604.41	0.456	1.37
	<220>	28.2	905.02	517.53	0.548	
Perovskite + Water	<110>	14.0	1799.25	900.18	0.469	1.24
	<220>	28.2	1456.85	860.55	0.571	
Perovskite + s-SWNT	<110>	14.0	1799.25	492.46	0.448	1.58
	<220>	28.3	1456.85	374.86	0.539	

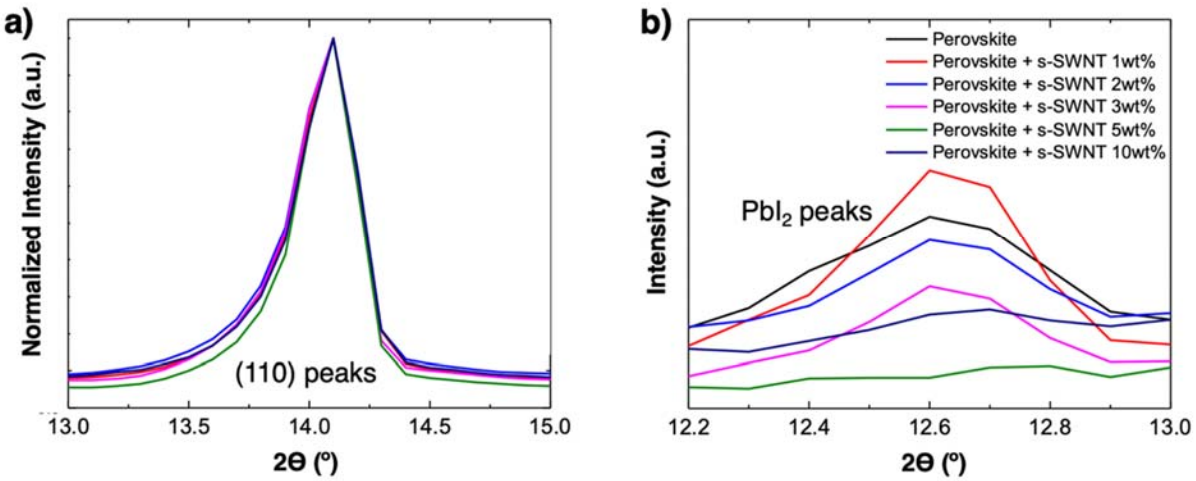

Figure S13. (a) Normalized (110) peak showing the FWHM trend of perovskite films with the increase in the s-SWNT concentration. (b) Magnified PbI_2 peaks of the perovskite films with the increase in the s-SWNT concentration.

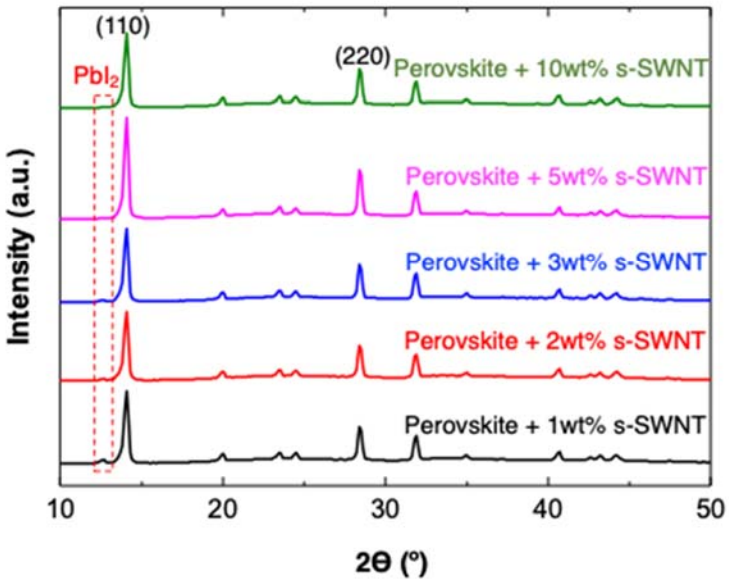

Figure S14. XRD spectra of perovskite films with the increase in the s-SWNT concentration.

Table S5. XRD peak characterizations and information for the s-SWNT-added $MAPbI_3$ film with varying $s\text{-}SWNT_{(aq)}$ concentrations.

Sample	Peak	Position (°)	Intensity	Peak Area	FWHM	Peak Ratio
Perovskite + 1wt% s-SWNT	<110>	14.1	374653	39607	0.401	2.18
	<220>	28.4	320750	15818	0.388	
Perovskite + 2wt% s-SWNT	<110>	14.1	501915	37888	0.398	2.16
	<220>	28.4	451442	15172	0.402	
Perovskite + 3wt% s-SWNT	<110>	14.1	637150	39691	0.392	2.19
	<220>	28.4	582173	15736	0.403	
Perovskite + 5wt% s-SWNT	<110>	14.1	813492	51066	0.388	2.24
	<220>	28.4	734450	20489	0.386	
Perovskite + 10wt% s-SWNT	<110>	14.1	948474	39449	0.391	2.13
	<220>	28.4	894635	16531	0.385	

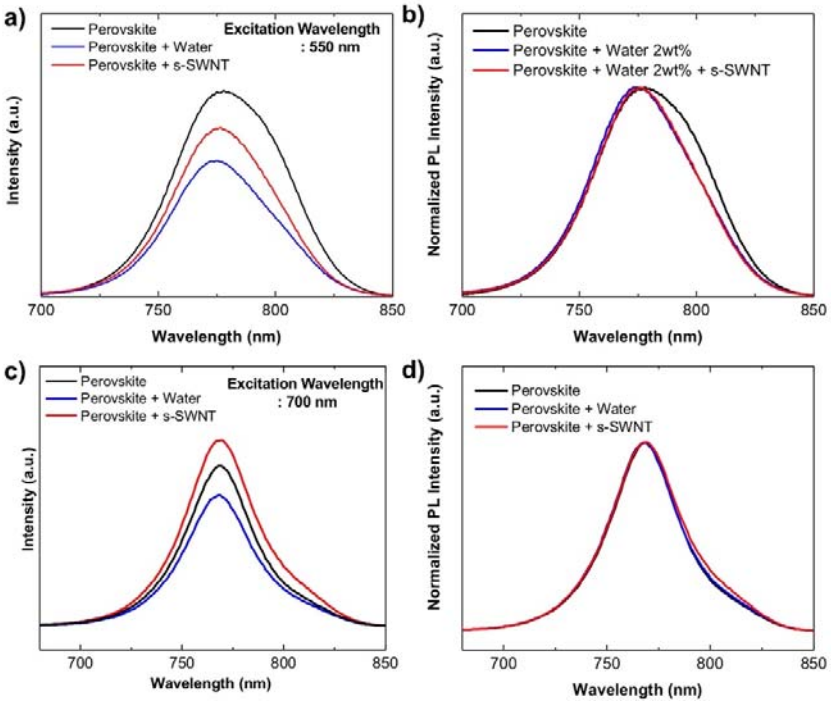

Figure S15. (a),(c) Raw and (b),(d) their normalized PL spectra with the different excitation wavelength of the reference $MAPbI_3$ films (black), the water-added $MAPbI_3$ films (blue), and the s-SWNT-added $MAPbI_3$ films (red).

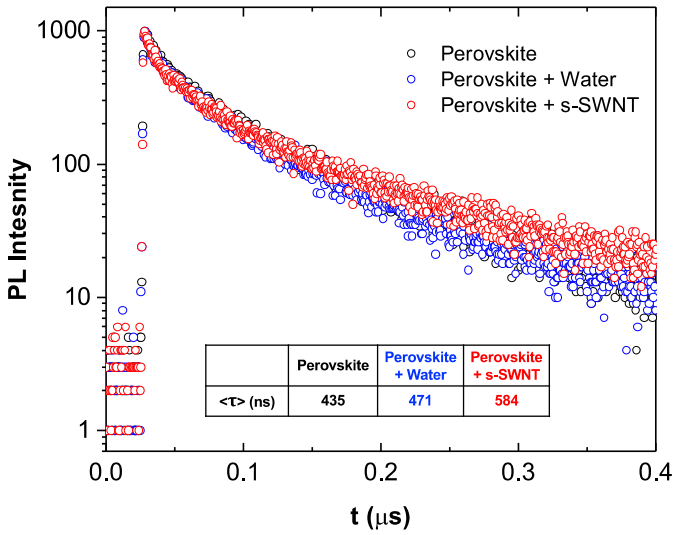

Figure S16. Time-resolved PL spectra of the reference $MAPbI_3$ films (black), the water-added $MAPbI_3$ films (blue), and the s-SWNT-added $MAPbI_3$ films (red).

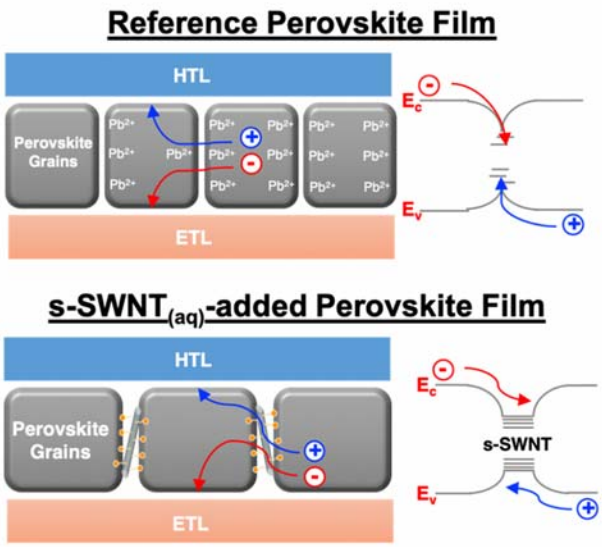

Figure S17. Cross-sectional illustration of MAPbI3 films (above) and the s-SWNT-added MAPbI3 films (below).

Table S6. Photovoltaic performance of the DOC-added PSCs.

DOC concentration	J_{SC} (mA cm^{-2})	V_{OC} (V)	FF	R_S (Ω cm^2)	PCE_{best} (%)	$PCE_{average}$ (%)
0.1 wt%	9.82	1.02	0.33	567	3.38	2.85 ±0.37
1.00 wt%	8.72	0.95	0.27	671	2.21	1.77 ±0.32

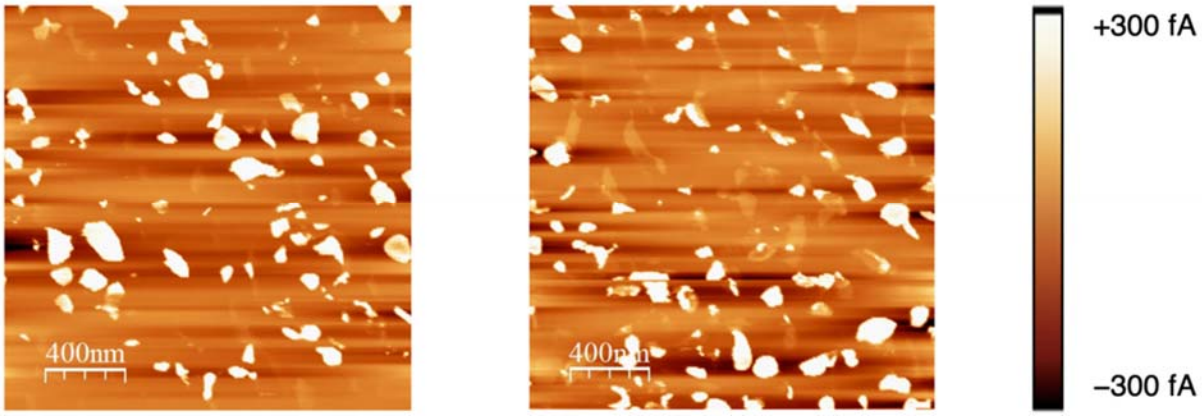

Figure S18. Conductive AFM images of the water-added $MAPbI_3$ films (left), and the s-SWNT-added $MAPbI_3$ films (right).

Table S7. EIS parameters for the PSCs of the reference $MAPbI_3$, the water-added $MAPbI_3$, and the s-SWNT added $MAPbI_3$.

Sample	Rs (Ω)	Rct (Ω)
Perovskite (ref.)	24.3	248.3
Perovskite + Water	82.1	121.2
Perovskite + s-SWNT	45.3	95.8

Table S8. Photovoltaic performance of the m-SWNT-added PSCs.

m-SWNT concentration	J_{SC} (mA cm^{-2})	V_{OC} (V)	FF	R_S (Ω cm^2)	PCE_{best} (%)	$PCE_{average}$ (%)
2 wt%	15.28	0.91	0.47	44.4	1.43x10^2	6.6

References

1. T. Tanaka, Y. Urabe, D. Nishide, H. Kataura, *Appl. Phys. Express,* 2009, **2**, 125002.

2. T. Tanaka, Y. Urabe, D. Nishide, H. Liu, S. Asano, S. Nishiyama, H. Kataura, *Phys. Status Solidi B*, 2010, **247**, 2867–2870.